Article

Rational design of anti-freezing electrolytes for extremely low-temperature aqueous batteries

Liwei Jiang [1,2,3,7], Shuai Han[1,2,7], Yuan-Chao Hu[4,7], Yang Yang [1,2], Yaxiang Lu [1,5] ✉, Yi-Chun Lu [3] ✉, Junmei Zhao [6] ✉, Liquan Chen[1] & Yong-Sheng Hu [1,2,5] ✉

Designing anti-freezing electrolytes through choosing suitable H_2O–solute systems is crucial for low-temperature aqueous batteries (LTABs). However, the lack of an effective guideline for choosing H_2O–solute systems based on decisive temperature-limiting factors hinders the development of LTABs. Here we identified two decisive factors: thermodynamic eutectic temperature (T_e) and kinetic glass-transition temperature (T_g), with T_g being applicable for LTABs only when H_2O–solute systems have strong super-cooling ability. We proposed a general strategy wherein low-T_e and strong-super-cooling ability electrolytes can be realized by creating multiple-solute systems via introducing assisted salts with high ionic-potential cations (for example, Al^{3+}, Ca^{2+}) or cosolvents with high donor numbers (for example, ethylene glycol). As a demonstration in Na-based systems, we designed electrolytes with ultralow T_e (−53.5 to −72.6 °C) and T_g (−86.1 to −117.1 °C), showcasing battery performances including 80 Wh kg^{-1} and 5,000 cycles at 25 °C, and 12.5 Wh kg^{-1} at −85 °C. The work provides effective guidelines for the design of anti-freezing electrolytes for extremely low-temperature applications.

With the increasing demand for applications under extremely low-temperature conditions, such as those found in extreme climates, outer space and deep sea enviroments[1–5], extensive attention has been paid to the design of anti-freezing electrolytes for rechargeable batteries, particularly aqueous batteries, as the water is prone to freezing[6–9]. According to typical equilibrium and non-equilibrium H_2O–solute phase diagrams[6], the freezing temperatures of H_2O–solute systems involve three important terms for low-temperature applications: freezing point (T_f), eutectic temperature (T_e) and glass-transition temperature (T_g). The different roles and effects of T_f, T_e and T_g on low-temperature batteries are often overlooked in designing anti-freezing electrolytes, which hinders the development of extreme LTABs.

First, most researchers have focused on regulating electrolyte T_f via various approaches[10–15]. However, T_f is not the most important temperature-limiting factor for low-temperature batteries. For instance, the partially frozen Li$^+$, Na$^+$, K$^+$, Zn^{2+}, H$^+$ and/or Cl$^-$-based[16–21]
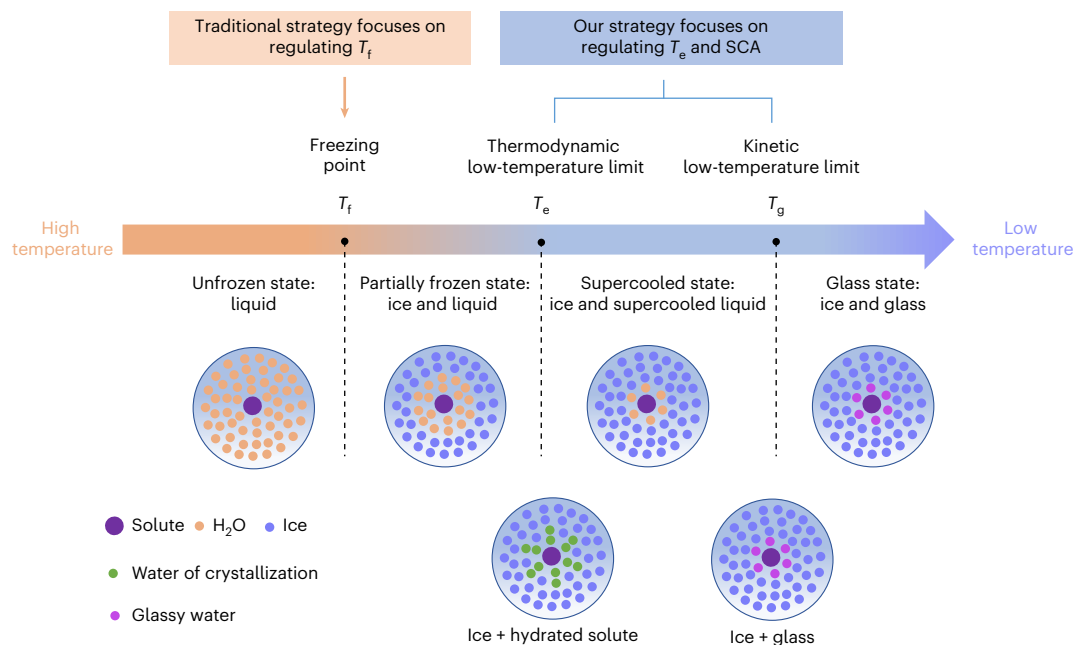
Fig. 1 | Schematic evolution of a dilute solution in the H_2O–solute system during cooling process and the difference between traditional and our proposed strategies. The freezing process involves several typical temperature terms of H_2O transitioning to ice (T_f), H_2O transitioning to the mixture of ice and water of crystallization (T_e), H_2O transitioning to glassy water (T_g).

aqueous electrolytes enable batteries to operate at temperatures below their T_f. According to a typical equilibrium H_2O–solute phase diagram[6], the T_e rather than the T_f is the thermodynamic decisive temperature-limiting factor for battery operation. As shown in Fig. 1, the T_f is the temperature at which an electrolyte begins to freeze and is in a partially frozen state, whereas the T_e is the temperature at which an electrolyte totally freezes. In a given H_2O–solute system[6], electrolytes with varying concentrations usually have different T_f, but they would have the same T_e. The T_f is usually not lower than the T_e ($T_f \geq T_e$; T_f equals T_e only when electrolyte concentration is the same as the eutectic-point concentration in equilibrium H_2O–solute phase diagram[6]). At temperatures below T_f, a dilute electrolyte usually becomes a mixture of ice and concentrated electrolyte (Fig. 1), and the mixture could still remain at a high enough ionic conductivity owing to the connected liquid region[17] before it is totally frozen as the crystalline state at T_e. Therefore, it is crucial to design anti-freezing electrolytes by choosing low-T_e H_2O–solute systems for extremely low-temperature applications.

Second, some anti-freezing electrolytes[22] exhibit ultralow T_g heat-flow steps on the differential scanning calorimetry (DSC) curves. However, T_g is a kinetic decisive temperature-limiting factor for low-temperature batteries and is only applicable for H_2O–solute systems with strong super-cooling ability (SCA). For instance, the 7 mol kg^{-1} (m) LiCl electrolytes have a T_f of −58 °C and a T_e of −74 °C according to the equilibrium H_2O–LiCl phase diagram[23], but it was reported to enable aqueous battery operation at −78 °C (ref. 20). This should be attributed to the strong SCA of H_2O–LiCl system. The concentrated solution in the H_2O–LiCl system can maintain a super-cooling liquid state at temperatures between its T_e (−74 °C)[23] and T_g (−132.5 °C)[24]. Similarly, the 9.5 m H_3PO_4 (T_e = −85 °C)[25] and 7.5 m $ZnCl_2$ (T_e = −63 °C)[26] can support aqueous batteries to operate at −88 °C (ref. 27) and −90 °C (ref. 22), respectively, which are also attributed to the strong SCA of H_2O–H_3PO_4 and H_2O-$ZnCl_2$ systems. According to the non-equilibrium H_2O–solute phase diagram[6], the lowest temperature at which an electrolyte can maintain a super-cooling liquid state is the T_g. The electrolytes in weak- and strong-SCA H_2O–solute systems both have T_e and T_g, with T_g being much lower than T_e. However, electrolytes in weak-SCA H_2O–solute systems cannot support a battery to operate at temperatures below T_e

because they will rapidly enter a crystalline state (which would therefore decrease the ionic conductivity) below T_e. In contrast, the electrolytes in strong-SCA H_2O–solute systems can maintain a super-cooling liquid state for a long time[6] at temperatures between T_e and T_g, and they may still remain at a high enough ionic conductivity at temperatures above T_g, thus enabling a battery to operate at temperatures between T_e and T_g. Therefore, the T_g serves as the kinetic decisive temperature-limiting factor for low-temperature battery operation, and it is only applicable for batteries using a strong-SCA electrolyte. It is crucial to design anti-freezing electrolytes by choosing strong-SCA H_2O–solute systems for extremely low-temperature applications.

Here, in contrast to the traditional strategy that focuses on regulating T_f, we focused on regulating T_e and SCA to design low-T_e and strong-SCA electrolytes for extremely low-temperature applications (Fig. 1). We discovered a general rule that H_2O–salt systems with high ionic-potential cations and H_2O–solvent systems with high solvent donor numbers usually have a strong SCA, according to many DSC experiments. Moreover, we proposed a general strategy whereby low-T_e and strong-SCA electrolytes can be realized by creating multiple-solute systems via introducing assisted salts with high ionic-potential cations (for example, Al^{3+}, Ca^{2+}) or cosolvents with high donor numbers (for example, ethylene glycol (EG)). As a demonstration in Na-based H_2O–solute systems, the designed low-T_e and strong-SCA 1 m $NaCF_3SO_3$ + 2.5 m $Al(CF_3SO_3)_3$ (Na–H_2O–Al), $H_{50}EG_{50}$-2 m $NaCF_3SO_3$ (Na–H_2O–EG) and 1 m $NaClO_4$ + 4 m $Ca(ClO_4)_2$ (Na–H_2O–Ca) electrolytes exhibit ultralow T_e (−53.5 to −72.6 °C) and T_g (−86.1 to −117.1 °C), with the low-T_e and strong-SCA mechanisms revealed to be related with electrolyte local structure coordination environments, H_2O–salt interactions, and complex competing ordering effects. The designed electrolytes enabled the superior performance of the $Na_{1.65}Fe_{0.21}Mn_{0.79}[Fe(CN)_6]_{0.92} \cdot 2.08H_2O$ (NaFeMnHCF)/Na–H_2O–EG/ $NaTi_2(PO_4)_3$ full cell (80 Wh kg^{-1} at 25 °C with 70% capacity retention over 5,000 cycles at 8 C, 63 Wh kg^{-1} at −60 °C and 0.05 C) and the NaFeMnHCF/Na–H_2O–Ca/3,4,9,10-perylenetetracarboxylic diimide (PTCDI) full cell (65.7 Wh kg^{-1} at 25 °C with 91.1% capacity retention over 250 cycles at 4 C, 20 Wh kg^{-1} at −80 °C and 0.1 C, and 12.5 Wh kg^{-1} at −85 °C and 0.1 C). This work marks an important development in
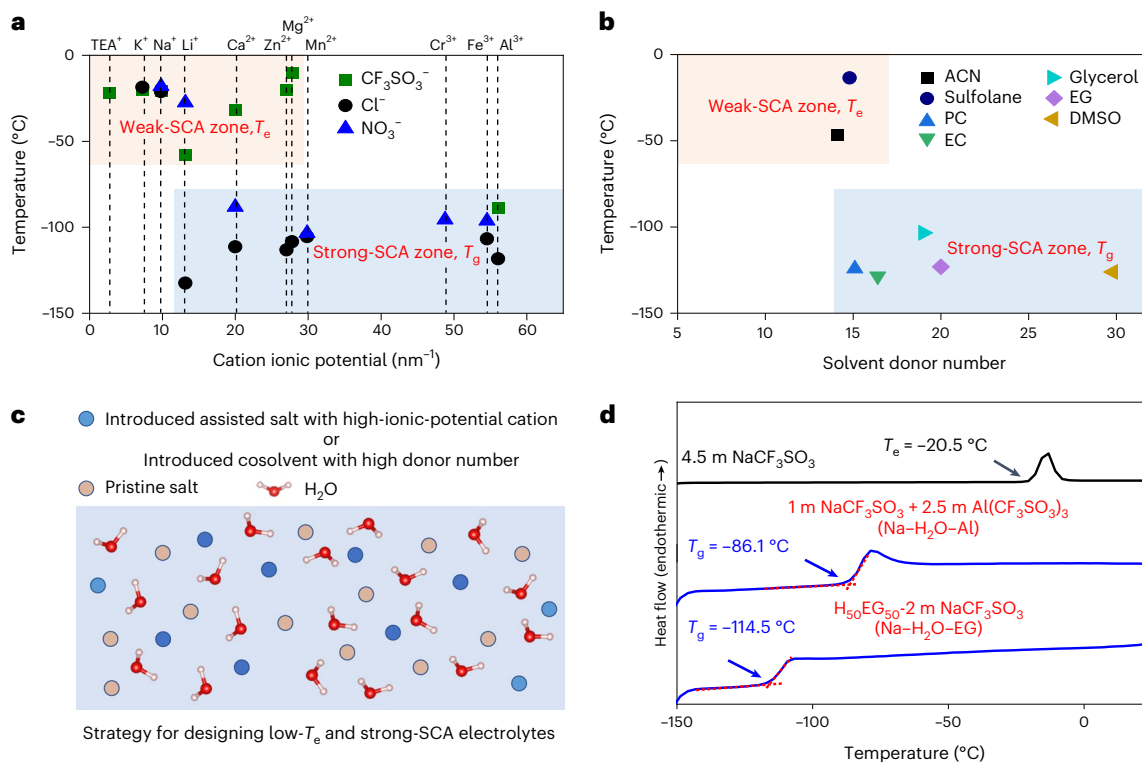
Fig. 2 | Design of low-T_e and strong-SCA aqueous electrolytes. a, The relationship of SCA attribute and cation ionic potential in various H_2O–salt systems. The weak-SCA and strong-SCA zones are identified by T_e heat-flow peak and T_g heat-flow step on the DSC heating curves, respectively. **b**, The relationship of SCA attribute and solvent donor number in various H_2O–solvent systems.

Solvents used were ACN, sulfolane, propylene carbonate (PC), ethylene carbonate (EC), glycerol, EG and dimethylsulfoxide (DMSO). **c**, Schematic illustration of the proposed general strategy for designing low-T_e and strong-SCA electrolytes. **d**, The DSC heating curves of 4.5 m $NaCF_3SO_3$ electrolytes, 1 m $NaCF_3SO_3$ + 2.5 m $Al(CF_3SO_3)_3$ (Na–H_2O–Al) and $H_{50}EG_{50}$-2 m $NaCF_3SO_3$ (Na–H_2O–EG) electrolytes.

anti-freezing electrolyte designs for extremely low-temperature applications.

Design low-T_e and strong-SCA aqueous electrolytes

To develop an effective guideline for designing low-T_e and strong-SCA aqueous electrolytes, we first examined what kind of H_2O–solute systems will have strong SCA. From DSC heating curves (see Supplementary Note 1 and Supplementary Fig. 1a–c for the conventional DSC analysis method[24,28,29]), one can observe a heat-flow signal of T_e or T_g for dilute solutions in an H_2O–solute system and identify its attribute (strong or weak) of SCA accordingly. The appearance of T_e heat-flow peak in an H_2O–solute system[30,31] indicates the weak SCA due to the complete crystallization during cooling, whereas the appearance of T_g heat-flow step[24,32] indicates the strong SCA because of the dominant glass state rather than the crystalline state during cooling. Therefore, a criterion can be proposed to distinguish weak- and strong-SCA H_2O–solute systems based on DSC data at a fixed cooling–heating rate: a dilution solution showing a T_e heat-flow peak and a T_g heat-flow step in DSC curve belong to the weak- and strong-SCA H_2O–solute systems, respectively (see examples in Supplementary Fig. 2a–c).

Although SCA attributes of a large number of H_2O–solute systems (the solute could be salt or cosolvent) can be obtained based on DSC data from the literature[24,31,32] and laboratory measurements (Supplementary Fig. 3a,b), there still lacks a guideline to directly design strong-SCA electrolytes through adjusting physicochemical parameters of H_2O–solute systems. Here, we discover that the ionic potentials of cations in salts and the donor numbers of cosolvents have a strong correlation with the SCA attribute (Fig. 2a,b and Supplementary Tables 1 and 2). For H_2O–salt systems (Fig. 2a), it is found that with the fixed anion of $CF_3SO_3^-$, most salts with low ionic-potential cations

(for example, K^+ 7.25 e nm^{-1}) fall into the weak-SCA zone, while the $Al(CF_3SO_3)_3$ salt with high ionic-potential cation (Al^{3+} 56.07 e nm^{-1}) falls into the strong-SCA zone. Other salts with fixed anions (Cl^- and NO_3^-) also obey a similar rule. For H_2O–solvent systems (Fig. 2b), it can be seen that solvents with low donor numbers, such as acetonitrile (ACN) (donor number 14.1), fall into the weak-SCA zone, whereas solvents with high donor numbers, such as the EG (donor number 20.0), fall into the strong-SCA zone. As a result, H_2O–salt systems with high ionic-potential cations and H_2O–solvent systems with high donor-number cosolvents are beneficial for systems falling into the strong-SCA zone.

In contrast to the SCA attribute that can be clearly correlated with the physicochemical parameters of H_2O–solute systems, it is difficult to find a similar rule for depicting the attribute (high or low) of T_e in H_2O–solute systems. Nevertheless, a low T_e can be realized by increasing the solute number because multiple-solute systems usually have lower T_e values than single-solute systems[33,34]. Therefore, we can propose a general design strategy for realizing low-T_e and strong-SCA electrolytes, which involves creating multiple-solute systems via introducing salts with high ionic-potential cations or cosolvents with high donor numbers, as illustrated in Fig. 2c.

To demonstrate the efficacy of the strategy proposed above, we take the Na-based system as an example to design low-T_e and strong-SCA electrolytes. Owing to the relatively low ionic potential of Na^+ (9.80 e nm^{-1}), most Na-based H_2O–salt electrolytes exhibit weak SCA, as demonstrated by the DSC data (Supplementary Fig. 4). The DSC results also show that most of Na-based H_2O–salt electrolytes have relatively high T_e (H_2O–Na_2SO_4 −1.2 °C, H_2O–$NaCF_3SO_3$ −20.5 °C, H_2O–$NaClO_4$ −34.1 °C and so on). Both features limit the aqueous Na-ion batteries to operate at extremely low temperatures. Therefore, it is crucial to design low-T_e and strong-SCA electrolytes for Na-based LTABs. Taking the H_2O–$NaCF_3SO_3$ system as an example, the DSC curves of
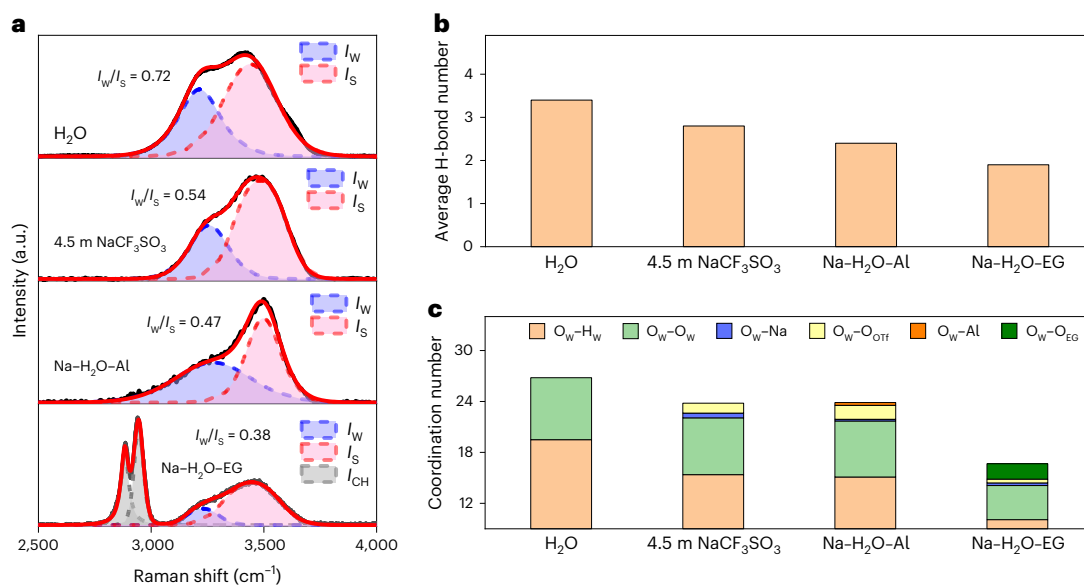
Fig. 3 | The low-T_e mechanisms in designed electrolytes. a, The fitted Raman spectra of H_2O, 4.5 m $NaCF_3SO_3$, Na–H_2O–Al and Na–H_2O–EG electrolytes from 2,500 to 4,000 cm^{-1} at 25 °C. **b**, The calculated average H-bond numbers in H_2O, 4.5 m $NaCF_3SO_3$, Na–H_2O–Al and Na–H_2O–EG structures. **c**, The coordination species and numbers (cut-off radius 4 Å) around O_W atom in various structures.

both dilute 10 wt% $NaCF_3SO_3$ (Supplementary Fig. 4) and eutectic-point concentration 4.5 m $NaCF_3SO_3$ electrolytes (Fig. 2d) demonstrate the high-T_e (−20.5 °C) and weak-SCA properties. When introducing a weak-SCA-zone KCF_3SO_3 salt or ACN cosolvent (Supplementary Fig. 5a,b), all the obtained electrolytes exhibit crystal melting heat-flow peaks and have no T_g heat-flow step, demonstrating that they failed to realize strong SCA. In comparison, when introducing strong-SCA-zone $Al(CF_3SO_3)_3$ salt or EG cosolvent into the H_2O–$NaCF_3SO_3$ system, all the obtained electrolytes exhibit T_g heat-flow steps (Fig. 2d and Supplementary Fig. 6a,b), demonstrating that they successfully realized strong SCA. It can be seen that the insufficient $Al(CF_3SO_3)_3$ salt or EG cosolvent results in cold crystallization heat-flow peak on the DSC heating curve, whereas an excess amount $Al(CF_3SO_3)_3$ salt or EG cosolvent leads to a high T_g value (Supplementary Fig. 6a,b). To ensure there is no cold crystallization and low T_g, 1 m $NaCF_3SO_3$ + 2.5 m $Al(CF_3SO_3)_3$ (Na–H_2O–Al; T_g = −86.1 °C) and $H_{50}EG_{50}$-2 m $NaCF_3SO_3$ (Na–H_2O–EG; T_g = −114.5 °C) are chosen as electrolytes for Na-based LTABs. In addition, the T_e of Na–H_2O–Al and Na–H_2O–EG electrolytes is estimated as −53.5 and −67.5 °C (Supplementary Fig. 6a,b), respectively, both of which are much lower than that of the H_2O–$NaCF_3SO_3$ system (−20.5 °C). As a result, we have been able to successfully design low-T_e and strong-SCA electrolytes by creating multiple-solute systems via introducing the $Al(CF_3SO_3)_3$ salt with high ionic-potential cation (Al^{3+} ionic potential 56.07 e nm^{-1}) or the EG cosolvent with high donor number (EG donor number 20.0) into the high-T_e and weak-SCA H_2O–$NaCF_3SO_3$ system. In addition to the example demonstrated above, we have included more examples regarding the designs of anti-freezing electrolytes in Na-based systems (Supplementary Figs. 7a,b and 8a,b and Supplementary Note 2), such as 1 m $NaClO_4$ + 4 m $Ca(ClO_4)_2$ (Na–H_2O–Ca) (T_e = −72.6 °C, T_g = −117.1 °C), demonstrating the general applicability of the proposed strategy.

Mechanisms of low T_e and strong SCA in designed electrolytes

To clarify why low-T_e and strong-SCA electrolytes can be efficiently designed using our proposed strategy in Fig. 2c, we performed Raman scattering and nuclear magnetic resonance (NMR) spectroscopy analyses as well as ab initio molecular dynamic (AIMD) simulations and density functional theory (DFT) calculations to the designed electrolytes, especially for Na–H_2O–Al and Na–H_2O–EG electrolytes.

Regarding the low T_e, this is associated with high electrolyte entropy based on the thermodynamic theory[6], namely a high degree of disorder in atomic coordination environment of electrolyte structures. The thermodynamic liquid-to-solid low-temperature limits are as follows: H_2O (0 °C) > 4.5 m $NaCF_3SO_3$ (−20.5 °C) > Na–H_2O–Al (about −53.5 °C) > Na–H_2O–EG (about −67.5 °C), indicating that the disorder of atomic coordination environment increases along the sequence. The mechanisms can be understood from two perspectives.

First, the degree of disorder of atomic coordination environment for different aqueous solutions can be reflected by the degree of hydrogen-bond (H-bond) breakage between water molecules, which can be studied by the OH stretching vibration (I_{OH}) bands between 3,000 and 4,000 cm^{-1} on Raman spectra and the average H-bond numbers based on AIMD statistical analyses. In pure water, the I_{OH} band is usually analysed by the two-state model including the hydrogen-bonded scatterers and non-hydrogen-bonded scatterers[35,36]. In aqueous solutions, the I_{OH} band can also be analysed by two factors including hydrogen-bonded scatterers and non-hydrogen-bonded (ion or solvent-hydrated) scatterers[37,38]. Here we use two Gaussian peaks (weak vibration band I_W and strong vibration band I_S, representing the predominant contribution of hydrogen- and non-hydrogen-bonded scatterers, respectively) to fit the I_{OH} bands (for the fitting in Na–H_2O–EG system, the additional two Gaussian peaks are used to represent the C–H vibration band I_{CH}; Fig. 3a) and define amplitude ratio (I_W/I_S) to reflect the degree of H-bond breakage (Fig. 3a). The order of I_W/I_S values is as follows: H_2O (0.72) > 4.5 m $NaCF_3SO_3$ (0.54) > Na–H_2O–Al (0.47) > Na–H_2O–EG (0.38), which is consistent with the order of liquid-to-solid low-temperature limits. Meanwhile, the AIMD results demonstrate that the average H-bond numbers between water molecules (Fig. 3b) show a similar order: H_2O (3.4) > 4.5 m $NaCF_3SO_3$ (2.8) > Na–H_2O–Al (2.4) > Na–H_2O–EG (1.9). A lower I_W/I_S value and a smaller average number of H-bonds indicate a higher degree of H-bond breakage and increased H-bond disorder within the electrolyte structure, which consequently leads to a lower liquid-to-solid low-temperature limit.

Second, the degree of disorder in different aqueous solutions can also be reflected by the coordination species and numbers around the O_W (oxygen atom in water) atoms. According to the AIMD simulation results (Fig. 3c, Supplementary Fig. 9a–f and Supplementary Table 3),
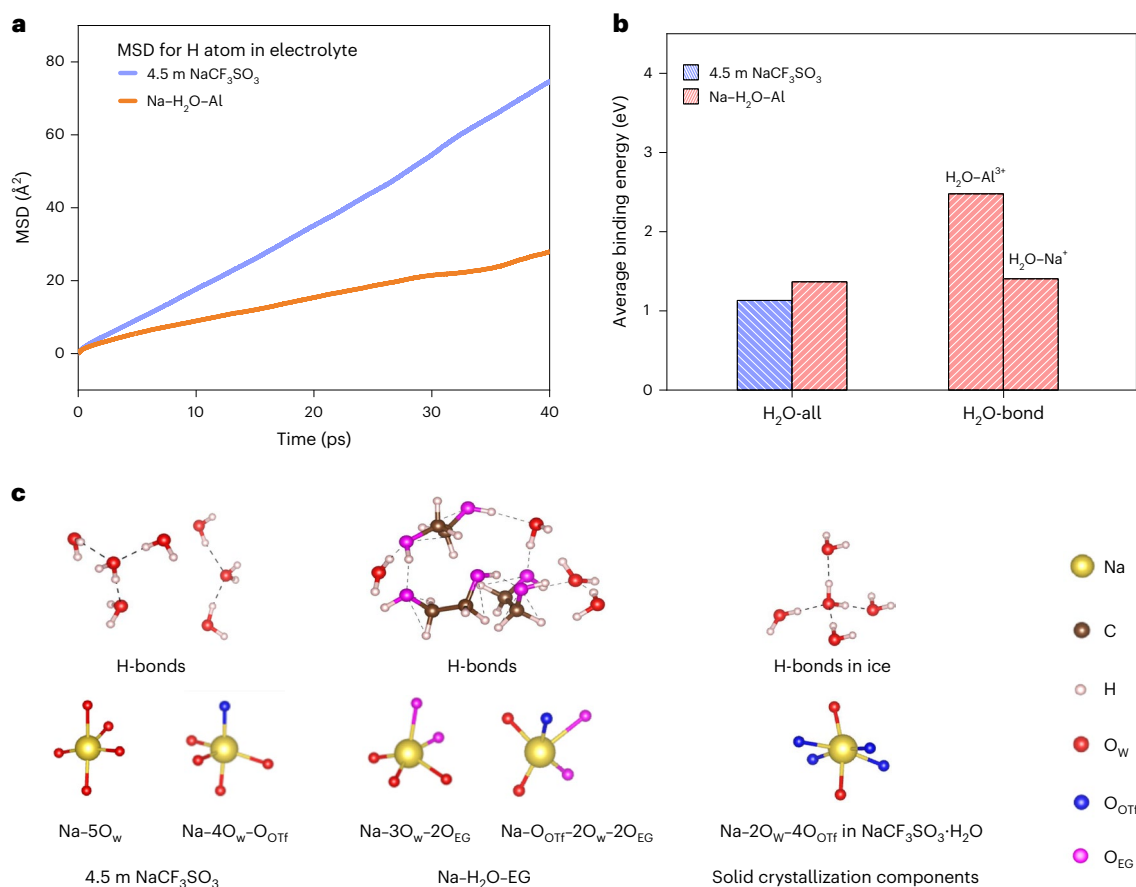
Fig. 4 | The strong-SCA mechanisms in designed electrolytes. a, Mean squared displacement (MSD) of the H atom at 300 K in 4.5 m $NaCF_3SO_3$ and $Na–H_2O–Al$ electrolytes. **b**, The calculated average binding energy of H_2O molecules in 4.5 m $NaCF_3SO_3$ and $Na–H_2O–Al$ electrolytes. H_2O-all, all H_2O molecules in electrolytes. H_2O-bond, H_2O molecules bonded with Na^+ ($H_2O–Na^+$) or Al^{3+} ($H_2O–Al^{3+}$) in a $Na–H_2O–Al$ electrolyte. **c**, Typical local structures for liquid electrolytes (4.5 m $NaCF_3SO_3$ and $Na–H_2O–EG$) and solid crystallization components (ice and $NaCF_3SO_3·H_2O$). The dotted line denotes the H-bond.

the pure H_2O has only two coordination species around the O_W atom ($O_W–H_W$ (hydrogen atom in water) and $O_W–O_W$) with respective coordination numbers of 19.5 and 7.4 in a cut-off radius of 4 Å. In comparison to pure H_2O, O_W atoms in 4.5 m $NaCF_3SO_3$ structure not only exhibit different coordination numbers (15.4 and 6.7) for the ordinary coordination species ($O_W–H_W$ and $O_W–O_W$), but also show two new coordination species ($O_W–Na$ and $O_W–O_{OTf}$ (oxygen atom in a CF_3SO_3 anion)) with coordination numbers of 0.6 and 1.2, respectively. Regarding the $Na–H_2O–Al$ and $Na–H_2O–EG$ electrolytes, the above-mentioned $O_W–H_W$, $O_W–O_W$, $O_W–Na$ and $O_W–O_{OTf}$ coordination species also exist but with different coordination numbers (Supplementary Table 3). Also, new species of $O_W–Al$ (coordination number 0.3) and $O_W–O_{EG}$ (oxygen atom in an EG molecule) (coordination number 1.8) appear, respectively (Supplementary Table 3). Therefore, the designed $Na–H_2O–Al$ and $Na–H_2O–EG$ electrolytes have more complex and diverse atomic coordination environments than the 4.5 m $NaCF_3SO_3$ electrolyte, thus resulting in a degree of higher disorder and lower T_c.

Regarding the strong SCA, this is associated with a strong frustration against crystallization process at low temperatures[39], which involves strong H_2O–solute interaction and a complex competing ordering effect, with the latter being a well-known mechanism in the field of metallic glasses[40,41]. The strong-SCA mechanisms of $Na–H_2O–Al$ and $Na–H_2O–EG$ electrolytes should be understood from different perspectives because salt and cosolvent have different properties. We revealed that the H_2O–salt interaction plays a dominant role in electrolytes containing high-ion-potential cations, whereas the complex competing ordering effect plays a dominant role in electrolytes containing high donor-number cosolvents.

For the $Na–H_2O–Al$ electrolyte, its strong-SCA mechanism can be interpreted by examining H_2O–solute interactions and the water diffusion kinetics using AIMD simulations, DFT calculations and two-dimensional diffusion-ordered NMR spectroscopy (2D-DOSY-NMR). As shown in Fig. 4a, the mean squared displacement of H atom in the $Na–H_2O–Al$ electrolyte is much lower than that in the 4.5 m $NaCF_3SO_3$ electrolyte within 40 ps, indicating slower water diffusion kinetics in the $Na–H_2O–Al$ electrolyte. The 2D-DOSY-NMR results (see the ^1H NMR spectra in Supplementary Fig. 10) further demonstrated that the $Na–H_2O–Al$ electrolyte has a lower ^1H diffusion coefficient ($4.1 × 10^{-10}$ $m^2 s^{-1}$) than the 4.5 m $NaCF_3SO_3$ electrolyte ($6.4 × 10^{-10}$ $m^2 s^{-1}$). This should be attributed to different H_2O–solute interactions in both electrolytes, which can be revealed by DFT calculations. As shown in Fig. 4b, the calculated average binding energy of H_2O molecules in $Na–H_2O–Al$ (1.37 eV) is higher than that of 4.5 m $NaCF_3SO_3$ (1.13 eV), which should be responsible for the lower ^1H diffusion coefficient in the $Na–H_2O–Al$ electrolyte. A higher average binding energy means that local atomic rearrangement for ice precipitation during the crystallization process is more difficult, thus resulting in a stronger SCA. We believe that after introducing $Al(CF_3SO_3)_3$ salt into an $H_2O–NaCF_3SO_3$ system, the increased average binding energy should be attributed to the higher ionic potential of Al^{3+} (56.07 e nm^{-1}) than Na^+ (9.80 e nm^{-1}). This can be demonstrated by the higher average binding energy of H_2O molecules bonded with Al^{3+} (2.48 eV of $H_2O–Al^{3+}$) than that of H_2O molecules bonded with Na^+ (1.41 eV of $H_2O–Na^+$) in the $Na–H_2O–Al$ electrolyte (Fig. 4b). In contrast, after introducing KCF_3SO_3 salt with a low ionic potential of K^+ (7.25 e nm^{-1}) into the $H_2O–NaCF_3SO_3$ system, the obtained 1 m $NaCF_3SO_3$ + 2.5 m KCF_3SO_3 ($Na–H_2O–K$) electrolyte

still has a weak SCA, which is attributed to a low H_2O molecule average binding energy (Supplementary Fig. 11 and Supplementary Note 3). These insights clarified why introducing a salt with high ionic-potential cation into the weak-SCA $H_2O-NaCF_3SO_3$ system can realize strong SCA.

For the Na–H_2O–EG electrolyte, its strong SCA can be understood by the complex competing ordering effect, which stems from local structure differences between liquid electrolyte and solid crystallization components[40,41]. AIMD simulations are adopted to examine the local structures with the assumption that both 4.5 m $NaCF_3SO_3$ and Na–H_2O–EG electrolytes would form the solid crystallization components containing ice and monohydrate $NaCF_3SO_3·H_2O$ crystals during the cooling process. Typical atomic-level local structures are extracted from the AIMD snapshots of 4.5 m $NaCF_3SO_3$ and Na–H_2O–EG electrolyte models as well as the experimental structures of ice and $NaCF_3SO_3·H_2O$ crystals (Fig. 4c and Supplementary Fig. 12a–d). The H-bond local structure difference between the Na–H_2O–EG electrolyte (diverse H-bond coordinating structures between H_2O and EG molecules) and ice crystal (four H-bond coordinating structures) is more noticeable than the difference between the 4.5 m $NaCF_3SO_3$ electrolyte (two or three H-bond coordinating structures) and ice crystal. Similarly, the Na–H_2O–EG electrolyte also exhibits a greater Na-coordination local structure difference (Na–$3O_W$–$2O_{EG}$ and Na–O_{OTf}^-–$2O_W$–$2O_{EG}$) to the $NaCF_3SO_3·H_2O$ crystal (Na–$2O_W$–$4O_{OTf}$) than that of the 4.5 m $NaCF_3SO_3$ electrolyte (Na–$5O_W$ and Na–$4O_W$–O_{OTf}) to the $NaCF_3SO_3·H_2O$ crystal. The greater the disparity in local structure between liquid electrolytes and solid crystallization components, the longer the atomic diffusion distance during the electrolyte crystallization process[39], thus frustrating the crystallization and resulting in a stronger SCA. The remarkably increased local structure difference between designed electrolyte and solid crystallization components after introducing the EG solvent into the $H_2O-NaCF_3SO_3$ system should be attributed to the high donor number (20.0) of the EG solvent, which is beneficial for coordinating with H_2O and Na^+. In contrast, after introducing the low donor-number (14.1) ACN cosolvent into the $H_2O-NaCF_3SO_3$ system, the obtained $H_{50}ACN_{50}$-2 m $NaCF_3SO_3$ (Na–H_2O–ACN) electrolyte still has a weak SCA, which should be attributed to the weak coordinating ability of the ACN molecule with H_2O and Na^+ (Supplementary Fig. 13 and Supplementary Note 3). These insights clarified why adding a high donor-number cosolvent into the weak-SCA $H_2O-NaCF_3SO_3$ system can result in a strong SCA.

In short, the mechanisms of low-T_e and strong-SCA properties are mainly associated with the local structure coordination environment, H_2O–salt interactions and complex competing ordering effects. The introduced assisted salts or cosolvents can increase electrolyte entropy by breaking H-bonds and enriching local structure coordination species, thus realizing low T_e. The assisted salts with high cation ionic potentials can enhance the H_2O–solute interaction, whereas the cosolvents with high donor numbers can increase local structure difference between the liquid electrolyte and solid crystallization components, both of which lead to strong frustration against crystallization process at low temperatures, thus realizing a strong SCA. These insights rationalize the low T_e and strong SCA of designed electrolytes as well as the proposed general design strategy for anti-freezing electrolytes in Fig. 2c.

Battery demonstrations for designed electrolytes

To show battery performance using the designed electrolytes at various temperatures, we synthesized the Prussian blue analogous cathode NaFeMnHCF (chemical formula $Na_{1.65}Fe_{0.21}Mn_{0.79}[Fe(CN)_6]_{0.92}·2.08H_2O$) and prepared two anode materials: a polyanionic anode $NaTi_2(PO_4)_3$ for achieving high energy density and an organic anode PTCDI for realizing ultralow temperature operation. The structural and compositional characterizations of electrode materials are depicted in Supplementary Figs. 14–17, Supplementary Tables 4 and 5 and Supplementary Note 4.

We examined the performance of NaFeMnHCF//$NaTi_2(PO_4)_3$ full cells in various electrolytes and temperatures. For full cells using the weak-SCA 4.5 m $NaCF_3SO_3$, Na–H_2O–K and Na–H_2O–ACN electrolytes,

the lowest operating temperatures are not lower than the T_e of these electrolytes, which are −20.5, −26.3 and −53.1 °C, respectively (Supplementary Fig. 18a–c). Since the weak-SCA electrolytes would rapidly become crystalline at temperatures below their T_e, the ion diffusions in these electrolytes are completely prevented. In contrast, benefiting from low T_e and strong SCA, both Na–H_2O–Al (T_e = −53.5 °C, T_g = −86.1 °C) and Na–H_2O–EG (T_e = −67.5 °C, T_g = −114.5 °C) electrolytes have high enough ionic conductivities at ultralow temperatures (Supplementary Table 6), enabling the NaFeMnHCF//$NaTi_2(PO_4)_3$ full cells to deliver reversible capacities at temperatures from −60 to 25 °C and even light bulbs at −70 °C (Fig. 5a–c and Supplementary Fig. 18d).

The NaFeMnHCF//$NaTi_2(PO_4)_3$ full cells using the Na–H_2O–EG electrolyte exhibited a much better performance than those using the Na–H_2O–Al electrolyte. In the Na–H_2O–Al electrolyte, the full cells show limited lifespans at −60 to 25 °C (4–14 cycles) (Supplementary Fig. 19a), which are much lower than full cells in the Na–H_2O–EG electrolyte (27–5,000 cycles) (Fig. 5a–c). The full cells using the Na–H_2O–Al electrolyte have issues of Al^{3+}-ion insertion on the cathode side (Supplementary Fig. 19b) and severe H_2 evolution on the anode side (the Na–H_2O–Al electrolyte pH value is roughly 4), whereas full cells using the Na–H_2O–EG electrolyte do not exhibit these issues. In addition, the Na–H_2O–EG electrolyte has lower T_e and T_g, wider voltage window and higher low-temperature ionic conductivity than the Na–H_2O–Al electrolyte (Supplementary Fig. 20a,b and Supplementary Table 6). Therefore, we focused on the performance of NaFeMnHCF//$NaTi_2(PO_4)_3$ full cells using the Na–H_2O–EG electrolyte at various temperatures. At 25 °C, the NaFeMnHCF/Na–H_2O–EG/$NaTi_2(PO_4)_3$ full cell delivers an energy density of 80 Wh kg^{-1} at 2 C, maintains 88% capacity retention from 2 to 10 C and exhibits 70% capacity retention at 8 C over 5,000 cycles (Fig. 5c and Supplementary Fig. 21a). At −40 °C, the full cell delivers an energy density of 72 Wh kg^{-1} at 0.1 C, maintains 68% capacity retention from 0.1 to 0.5 C and shows 96% capacity retention after 80 cycles at 0.5 C (Supplementary Fig. 21b,c). At −60 °C, the full cell delivers an energy density of 63 Wh kg^{-1} at 0.05 C and maintains 65% capacity retention from 0.05 to 0.15 C (Fig. 5b and Supplementary Fig. 21d).

To demonstrate an aqueous Na-ion battery with a more impressive low-temperature performance, we assembled the NaFeMnHCF//PTCDI full cell using the designed Na–H_2O–Ca electrolyte (T_e = −72.6 °C, T_g = −117.1 °C). Benefiting from the high ionic conductivity of the electrolyte (112.5 mS cm^{-1} at 25 °C, 0.8 mS cm^{-1} at −80 °C; Supplementary Table 6), the NaFeMnHCF/Na–H_2O–Ca/PTCDI full cell can stably operate at temperatures ranging from 25 to −85 °C. We examined the performance of both coin and pouch cells at various temperatures (Fig. 5d,e and Supplementary Figs. 22a–d and 23a–c). At 25 °C, the coin cell delivers a high energy density of 65.7 Wh kg^{-1} and remains at 91.1% capacity retention over 250 cycles at 4 C (Supplementary Fig. 22a,b). At −60 °C, the coin cell delivers a high energy density of 46.3 Wh kg^{-1} and remains at 85.1% capacity retention over 70 cycles at 0.5 C (Supplementary Fig. 22c,d). At −80 °C, the coin cell delivers a high energy density of 20 Wh kg^{-1} and remains at 93.1% capacity retention over 20 cycles at 0.1 C (Fig. 5e and Supplementary Fig. 23a). At −85 °C, the coin cell delivers an energy density of 12.5 Wh kg^{-1} at 0.1 C (Supplementary Fig. 23b). As shown in Fig. 5d and Supplementary Fig. 23c, the assembled pouch cell delivers 10.4, 6.9, 4.9 and 2.3 mAh at 25, −60, −80 and −85 °C, respectively. Compared with reported aqueous Na-ion batteries[13,15,42–46] (Supplementary Fig. 24 and Supplementary Table 7), our demonstrated full cells achieve the best overall performance in terms of energy density, cycling lifespan and lower limit of operating temperature.

Conclusions

In summary, we recognized two liquid-to-solid low-temperature limits (T_e and T_g) of H_2O–solute systems, as well as the importance of designing anti-freezing electrolytes by choosing low-T_e and strong-SCA H_2O–solute systems for extremely low-temperature applications. We proposed a general strategy that low-T_e and strong-SCA electrolytes can be realized
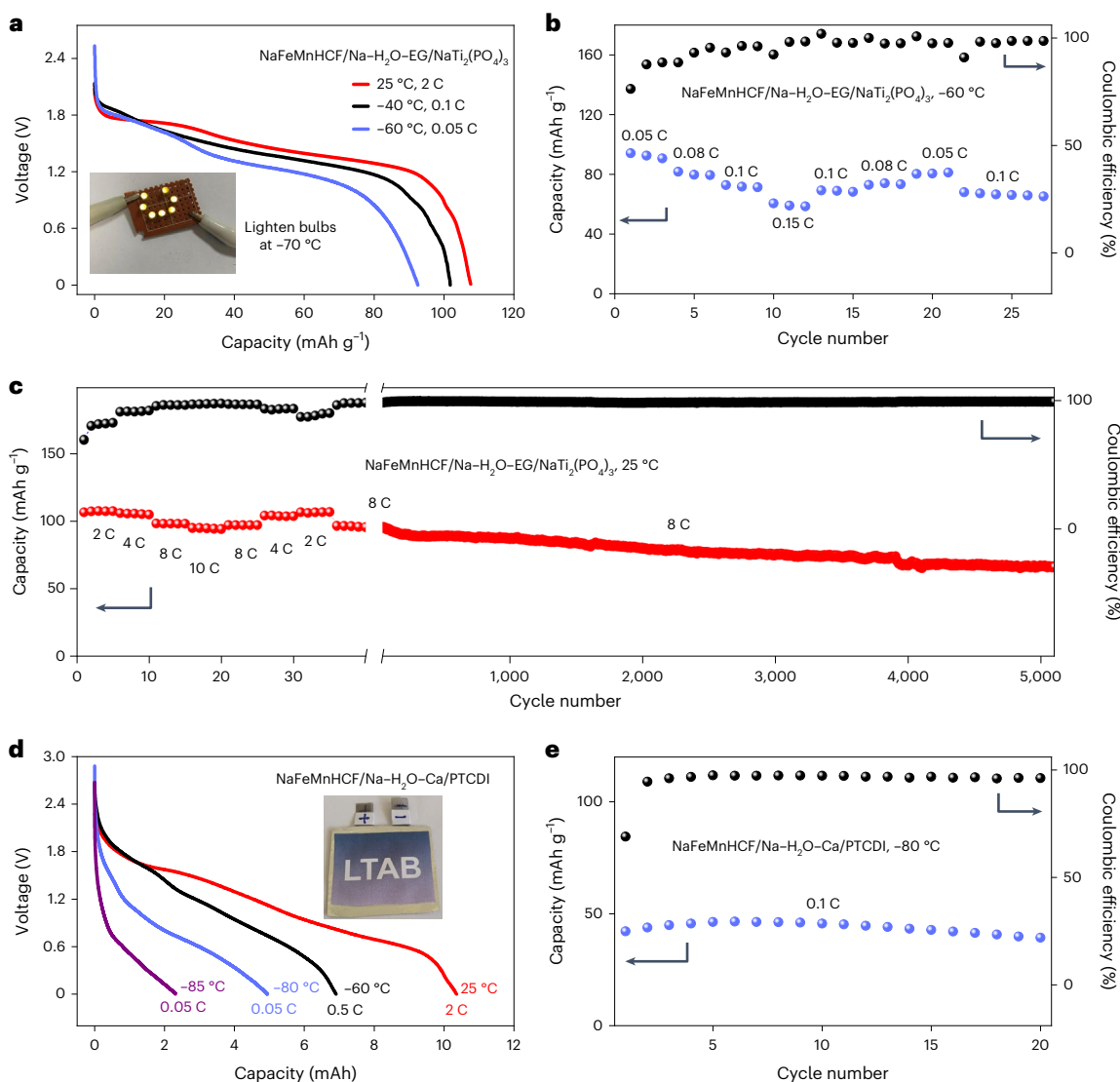
Fig. 5 | Battery demonstrations in designed electrolytes. a, The discharge curves of the NaFeMnHCF/Na–H$_2$O–EG/NaTi$_2$(PO$_4$)$_3$ full cell at various temperatures. The inset photograph shows the bulbs lighted by full cells at −70 °C. **b,c**, Rate capability and cycling stability of the NaFeMnHCF/Na–H$_2$O–EG/ NaTi$_2$(PO$_4$)$_3$ full cell at −60 °C (**b**) and 25 °C (**c**). **d**, Typical discharge curves of NaFeMnHCF/Na–H$_2$O–Ca/PCDI pouch cell at temperatures ranging from −85 to 25 °C. The inset is a photograph of the assembled pouch cell. **e**, Cycling stability of a NaFeMnHCF/Na–H$_2$O–Ca/PCDI coin cell at −80 °C and 0.1 C.

by creating multiple-solute systems via introducing assisted salts with high ionic-potential cations or cosolvents with high donor numbers. Taking the Na-based system as an example, the designed low-T_e and strong-SCA Na–H$_2$O–Al, Na–H$_2$O–EG and Na–H$_2$O–Ca electrolytes show ultralow T_e (−53.5 to −72.6 °C) and T_g (−86.1 to −117.1 °C), enabling the superior performance of the NaFeMnHCF/Na–H$_2$O–EG/NaTi$_2$(PO$_4$)$_3$ full cell (80 Wh kg^{-1} at 25 °C with 70% capacity retention over 5,000 cycles at 8 C, 63 Wh kg^{-1} at −60 °C and 0.05 C) and the NaFeMnHCF/Na–H$_2$O–Ca/ PTCDI full cell (65.7 Wh kg^{-1} at 25 °C with 91.1% capacity retention over 250 cycles at 4 C, 20 Wh kg^{-1} at −80 °C and 0.1 C, 12.5 Wh kg^{-1} at −85 °C and 0.1 C). The mechanisms of low-T_e and strong-SCA properties are revealed to be associated with local structure coordination environment, H$_2$O–salt interaction and a complex competing ordering effect. This work provides an effective guideline for anti-freezing electrolyte designs, marking an important development for extreme LTABs.

Methods
Materials and electrolytes
The NaFeMnHCF cathode was prepared by a simple precipitation method. Typically, 2 mmol Na$_4$Fe(CN)$_6$·10H$_2$O and a corresponding

proportion of FeSO$_4$·7H$_2$O (0.4 mmol) and MnSO$_4$·H$_2$O (1.6 mmol) were dissolved into 100 and 80 ml of H$_2$O–EG hybrid solution (equal volume), respectively. Then, the latter solution was slowly dropped into the former with magnetic stirring at room temperature. After 12 h, the precipitate formed was centrifuged and washed thoroughly with deionized water. The final product was obtained after drying in air under 80 °C for 12 h. The NaTi$_2$(PO$_4$)$_3$ was synthesized through the sol-gel method according to the literature[47]. The PTCDI powder (CAS number 81–33–4) was purchased from TCI Co., Ltd. The H$_x$EG$_y$-2 m NaCF$_3$SO$_3$ electrolyte was made by dissolving the 2 mmol NaCF$_3$SO$_3$ in 2 g of solvent (prepared by x% ml of H$_2$O and y% ml of EG). The 1 m NaCF$_3$SO$_3$ + 2.5 m Al(CF$_3$SO$_3$)$_3$ electrolyte was obtained by dissolving the 1 mmol NaCF$_3$SO$_3$ and 2.5 mmol Al(CF$_3$SO$_3$)$_3$ in 1 g H$_2$O. Other electrolytes were prepared in a similar way to the H$_x$EG$_y$-2 m NaCF$_3$SO$_3$ and 1 m NaCF$_3$SO$_3$ + 2.5 m Al(CF$_3$SO$_3$)$_3$ electrolytes.

Electrochemical measurements
The NaFeMnHCF and NaTi$_2$(PO$_4$)$_3$ electrodes were fabricated using active materials, carbon black and polytetrafluorothylene at a weight ratio of 7/2/1. The CR2032-type coin cells are used to assemble the

$NaFeMnHCF/Na–H_2O–EG/NaTi_2(PO_4)_3$ and $NaFeMnHCF/Na–H_2O–$ $Ca/PTCDI$ full cells (cathode/anode mass ratio was 1/0.9). The Swagelok-type cells (Ti foil was used to protect against proton corrosion) $NaFeMnHCF/Na–H_2O–Al/NaTi_2(PO_4)_3$ full cell (cathode/anode mass ratio was 1/1.5). The mass loading values for NaFeMnHCF and $NaTi_2(PO_4)_3$, and PTCDI electrodes in coin cells were about 5.2 and 4.1 mg cm^{-2}, respectively. The mass loading values for NaFeMnHCF and PTCDI electrodes in pouch cells were about 12.4 and 10.6 mg cm^{-2}, respectively. The reversible capacities of $NaFeMnHCF/Na–H_2O–EG/$ $NaTi_2(PO_4)_3$ and $NaFeMnHCF/Na–H_2O–Ca/PTCDI$ full cells are shown on the basis of cathode mass, whereas the reversible capacity of NaFeMn-$HCF/Na–H_2O–Al/NaTi_2(PO_4)_3$ full cell is displayed on the basis of anode mass. The energy densities of all full cells were calculated by total active mass of cathode and anode. All charge–discharge curves were performed using the NEWARE Battery Test System (catalogue no. CT-4008-5V50mA-164).

Material characterizations

DSC tests were carried out in DSC200F3 at a temperature range from 25 to −150 °C. All samples had mesophase carbon micro-beads added to promote nucleation[48]. The cooling–heating rates were 20 K min^{-1} (to keep to the same testing conditions of Cl-based and NO$_3$-based $H_2O–$salt systems in the literature[24]) for 10 wt% LiNO$_3$ and 10 wt% KCl aqueous solution samples. The cooling–heating rates of other samples were 10 K min^{-1}. The Raman spectroscopy for the electrolyte OH stretch was conducted on a HORIBA HR Evolution microscope using a 532 nm excitation laser. The ^{1}H 2D-DOSY-NMR spectra were produced using a Bruker DRX 600 spectrometer. The structures were characterized using an X'Pert Pro MPD X-ray diffractometer (D8 Bruker) with Cu $K_α$ radiation ($λ = 1.5405$ Å). X-ray photoelectron spectra were recorded with a spectrometer that had Mg/Al Kα radiation (ESCALAB 250 Xi, ThermoFisher). The morphologies of the electrodes were obtained by scanning electron microscopy (Hitachi-S4800). The thermogravimetric analysis for NaFeMnHCF cathode was conducted on a NETZSCH-STA449C thermal analysis device. The elemental ratios of Na, Fe and Mn in the NaFeMnHCF cathode were determined by inductively coupled plasma atomic emission spectrometry. For low-temperature tests, the cell performance was measured in ShangHai BoYi (B-T-107D and B-T-80-E) low-temperature ovens at temperatures ranging from −85 to 25 °C. The reference electrode for testing the electrochemical window at various temperatures was a Zn^{2+}/Zn electrode with 7.5 m ZnCl$_2$ electrolyte (−0.67 V versus a standard hydrogen electrode). Three $NaFeMnHC/Na–H_2O–EG/NaTi_2(PO_4)_3$ coin cells (fully charged at room temperature) were used to power light emitting diode bulbs at −70 °C. The ionic conductivities of electrolytes were measured via an electrochemical impedance spectrum using the Pt electrode equipment purchased from Shanghai Russell Technology Co., Ltd. The linear sweep voltammetry experiments were conducted using a VMP3 electrochemical testing unit (BioLogic).

Computations

The DFT calculations were carried out by using the Vienna ab initio simulation package[49]. The projector augmented-wave potentials[50] generated with Perdew–Burke–Ernzerhof generalized gradient approximation[51] were used. The van der Waals interaction was taken into account by using the rev-vdWDF2 functional[52]. The plane wave cut-off energy was set to 400 eV and the Γ point was used for the Brillouin zone sampling. The AIMD simulations were performed in a canonical ensemble (NVT) by using a Nosé thermostat[53,54], with a time step of 1 fs. All molecular dynamics simulations were run for 40 ps at 400 K first, then run for 20 ps at 300 K to yield the data for analysis. The water calculation model contained 55 H$_2$O molecules within a 11.8 × 11.8 × 11.8 Å^3 cubic supercell. The 4.5 m NaCF$_3$SO$_3$ electrolyte calculation model contained two NaCF$_3$SO$_3$ and 25 H$_2$O within a 10 × 10 × 10 Å^3 cubic supercell. The Na–H$_2$O–Al electrolyte calculation model contained one

NaCF$_3$SO$_3$, two Al(CF$_3$SO$_3$)$_3$ and 55 H$_2$O within a 13.5 × 13.5 × 13.5 Å^3 cubic supercell. The Na–H$_2$O–EG electrolyte calculation model contained two NaCF$_3$SO$_3$, nine (CH$_2$OH)$_2$ and 28 H$_2$O within a 13.0 × 13.0 × 13.0 Å^3 cubic supercell. The Na–H$_2$O–K electrolyte calculation model contained one NaCF$_3$SO$_3$, two KCF$_3$SO$_3$ and 55 H$_2$O within a 13.0 × 13.0 × 13.0 Å^3 cubic supercell. The Na–H$_2$O–ACN electrolyte calculation model contained two NaCF$_3$SO$_3$, ten CH$_3$CN and 31 H$_2$O within a 13.0 × 13.0 × 13.0 Å^3 cubic supercell. All initial electrolyte structures of calculation models were constructed using the Packmol software[55] according to the experimental density. The ice (mp-697111) and NaCF$_3$SO$_3$·H$_2$O (mp-601202) crystal structures comes from the website https://materialsproject.org/. The average binding energy of the H$_2$O molecule was calculated using DFT based on the structure of the AIMD snapshot. The binding energy of an H$_2$O molecule in electrolyte is calculated by the formula as follows: $E_b = E_{H_2O} + E^1_{electrolyte} − E^0_{electrolyte}$, where the E_b is the binding energy of the H$_2$O molecule in electrolytes, E_{H_2O} is energy of the H$_2$O molecule in a vacuum, $E^0_{electrolyte}$ is energy of the electrolyte structure model obtained by AIMD simulation and $E^1_{electrolyte}$ is energy of the calculation model whose water numbers are one less than the electrolyte model obtained by AIMD simulation. The average H-bond numbers were calculated on the basis of the geometrical criterion of O–H···O angle <30° and the distance of two O being less than 0.35 nm.

Data availability

The datasets analysed and generated during the current study are included in the paper and its Supplementary Information.

References

1. Xu, J. et al. Electrolyte design for Li-ion batteries under extreme operating conditions. *Nature* **614**, 694–700 (2023).
2. Rodrigues, M.-T. F. et al. A materials perspective on Li-ion batteries at extreme temperatures. *Nat. Energy* **2**, 17108 (2017).
3. Zhu, G. et al. Rechargeable Na/Cl$_2$ and Li/Cl$_2$ batteries. *Nature* **596**, 525–530 (2021).
4. Ai, F. et al. Heteropoly acid negolytes for high-power-density aqueous redox flow batteries at low temperatures. *Nat. Energy* **7**, 417–426 (2022).
5. Jiang, L. W., Hu, Y.-C., Ai, F., Liang, Z. J. & Lu, Y.-C. Rational design of anti-freezing electrolyte concentrations via freeze concentration process. *Energy Environ. Sci.* **17**, 2815–2824 (2024).
6. Jiang, L., Dong, D. & Lu, Y.-C. Design strategies for low temperature aqueous electrolytes. *Nano Res. Energy* **1**, e9120003 (2022).
7. Guo, Q., Han, S., Lu, Y., Chen, L. & Hu, Y.-S. Low-temperature aqueous Na-ion batteries: strategies and challenges of electrolyte design. *Chin. Phys. Lett.* **40**, 028801 (2023).
8. Yue, J. et al. Aqueous interphase formed by CO$_2$ brings electrolytes back to salt-in-water regime. *Nat. Chem.* **13**, 1061–1069 (2021).
9. Jiang, L. et al. Building aqueous K-ion batteries for energy storage. *Nat. Energy* **4**, 495–503 (2019).
10. Zhang, Q. et al. Chaotropic anion and fast-kinetics cathode enabling low-temperature aqueous Zn batteries. *ACS Energy Lett.* **6**, 2704–2712 (2021).
11. Tang, L. et al. Strengthening aqueous electrolytes without strengthening water. *Angew. Chem. Int. Ed.* **62**, e202307212 (2023).
12. Qiu, M. et al. Tailoring water structure with high-tetrahedral-entropy for antifreezing electrolytes and energy storage at −80°C. *Nat. Commun.* **14**, 601 (2023).
13. Zhu, K. et al. Inorganic electrolyte for low-temperature aqueous sodium ion batteries. *Small* **18**, 2107662 (2022).
14. Zhu, K. et al. Tailoring pure inorganic electrolyte for aqueous sodium-ion batteries operating at −60°C. *Batter. Supercaps.* **5**, e202200308 (2022).

15. Nian, Q. S. et al. Aqueous batteries operated at −50 °C. *Angew. Chem. Int. Ed.* **58**, 16994–16999 (2019).

16. Suo, L. et al. 'Water-in-salt' electrolytes enable green and safe Li-ion batteries for large scale electric energy storage applications. *J. Mater. Chem. A* **4**, 6639–6644 (2016).

17. Nian, Q. et al. Regulating frozen electrolyte structure with colloidal dispersion for low temperature aqueous batteries. *Angew. Chem. Int. Ed.* **62**, e202217671 (2023).

18. Sun, Y. et al. Salty ice electrolyte with superior ionic conductivity towards low-temperature aqueous zinc ion hybrid capacitors. *Adv. Funct. Mater.* **31**, 2101277 (2021).

19. Guo, Z. et al. An organic/inorganic electrode-based hydronium-ion battery. *Nat. Commun.* **11**, 959 (2020).

20. Sui, Y. et al. Reversible Cl_2/Cl^- redox for low-temperature aqueous batteries. *ACS Energy Lett.* **8**, 988–994 (2023).

21. Jiang, L. & Lu, Y.-C. Building a long-lifespan aqueous K-ion battery operating at −35 °C. *ACS Energy Lett.* **9**, 985–991 (2024).

22. Zhang, Q. et al. Modulating electrolyte structure for ultralow temperature aqueous zinc batteries. *Nat. Commun.* **11**, 4463 (2020).

23. Monnin, C., Dubois, M., Papaiconomou, N. & Simonin, J.-P. Thermodynamics of the LiCl⁺ H_2O system. *J. Chem. Eng. Data* **47**, 1331–1336 (2002).

24. Wang, Q., Zhao, L., Li, C. & Cao, Z. The decisive role of free water in determining homogenous ice nucleation behavior of aqueous solutions. *Sci. Rep.* **6**, 26831 (2016).

25. Corti, H. R., Nores-Pondal, F. J. & Angell, C. A. Heat capacity and glass transition in P_2O_5-H_2O solutions: support for Mishima's conjecture on solvent water at low temperature. *Phys. Chem. Chem. Phys.* **13**, 19741–19748 (2011).

26. Pillai, S. B., Wilcox, R. J., Hillis, B. G., Losey, B. P. & Martin, J. D. Understanding the water-in-salt to salt-in-water characteristics across the zinc chloride: water phase diagram. *J. Phys. Chem. B* **126**, 2265–2278 (2022).

27. Jiang, H. et al. A high-rate aqueous proton battery delivering power below −78 °C via an unfrozen phosphoric acid. *Adv. Energy Mater.* **10**, 2000968 (2020).

28. Gibout, S., Franquet, E., Haillot, D., Bédécarrats, J.-P. & Dumas, J.-P. Challenges of the usual graphical methods used to characterize phase change materials by differential scanning calorimetry. *Appl. Sci.* **8**, 66 (2018).

29. Ding, M., Xu, K. & Jow, T. Phase diagram of EC–DMC binary system and enthalpic determination of its eutectic composition. *J. Therm. Anal. Calorim.* **62**, 177–186 (2000).

30. Franquet, E., Gibout, S., Bédécarrats, J. P., Haillot, D. & Dumas, J. P. Inverse method for the identification of the enthalpy of phase change materials from calorimetry experiments. *Thermochim. Acta* **546**, 61–80 (2012).

31. Zhao, L., Pan, L., Cao, Z. & Wang, Q. Confinement-induced vitrification of aqueous sodium chloride solutions. *Chem. Phys. Lett.* **647**, 170–174 (2016).

32. Zhao, L. S., Cao, Z. X. & Wang, Q. Glass transition of aqueous solutions involving annealing-induced ice recrystallization resolves liquid-liquid transition puzzle of water. *Sci. Rep.* **5**, 15714 (2015).

33. Wang, X., Huang, W., Liu, F., Liu, N. & Huang, X. Determination and graphics expression of ice-salt eutectic points of the multicomponent electrolyte solutions. *Fluid Phase Equilib.* **458**, 115–122 (2018).

34. Yu, D., Xue, Z. & Mu, T. Eutectics: formation, properties, and applications. *Chem. Soc. Rev.* **50**, 8596–8638 (2021).

35. Walrafen, G. E. Raman spectral studies of the effects of temperature on water structure. *J. Chem. Phys.* **47**, 114–126 (1967).

36. Hare, D. E. & Sorensen, C. M. Raman spectroscopic study of bulk water supercooled to −33 °C. *J. Chem. Phys.* **93**, 25–33 (1990).

37. Wang, Y. H. et al. In situ Raman spectroscopy reveals the structure and dissociation of interfacial water. *Nature* **600**, 81–85 (2021).

38. Yang, B., Cao, X., Wang, C., Wang, S. & Sun, C. Investigation of hydrogen bonding in water/DMSO binary mixtures by Raman spectroscopy. *Spectrochim. Acta A Mol. Biomol. Spectrosc.* **228**, 117704 (2020).

39. Hu, Y.-C & Tanaka, H. Physical origin of glass formation from multicomponent systems. *Sci. Adv.* **6**, eabd2928 (2020).

40. Tanaka, H. Bond orientational order in liquids: towards a unified description of water-like anomalies, liquid–liquid transition, glass transition, and crystallization. *Eur. Phys. J. E* **35**, 113 (2012).

41. Hu, Y.-C. & Tanaka, H. Revealing the role of liquid preordering in crystallisation of supercooled liquids. *Nat. Commun.* **13**, 4519 (2022).

42. Jiang, L. et al. High-voltage aqueous Na-ion battery enabled by inert-cation-assisted water-in-salt electrolyte. *Adv. Mater.* **32**, 1904427 (2020).

43. Reber, D., Kühnel, R.-S. & Battaglia, C. Suppressing crystallization of water-in-salt electrolytes by asymmetric anions enables low-temperature operation of high-voltage aqueous batteries. *ACS Mater. Lett.* **1**, 44–51 (2019).

44. Wu, X. Y. et al. Energetic aqueous rechargeable sodium-ion battery based on $Na_2CuFe(CN)_6$–$NaTi_2(PO_4)_3$ intercalation chemistry. *Chem. Sus. Chem.* **7**, 407–411 (2014).

45. Fernández-Ropero, A. J., Saurel, D., Acebedo, B., Rojo, T. & Casas-Cabanas, M. Electrochemical characterization of $NaFePO_4$ as positive electrode in aqueous sodium-ion batteries. *J. Power Sources* **291**, 40–45 (2015).

46. Zhang, Y. et al. All-climate aqueous Na-ion batteries using 'water-in-salt' electrolyte. *Sci. Bull.* **67**, 161–170 (2022).

47. Yue, J. et al. Interface concentrated-confinement suppressing cathode dissolution in water-in-salt electrolyte. *Adv. Energy Mater.* **10**, 2000665 (2020).

48. Ding, M. S. & Xu, K. Phase diagram, conductivity, and glass transition of LITFSI–H_2O binary electrolytes. *J. Phys. Chem. C.* **122**, 16624–16629 (2018).

49. Kresse, G. & Furthmüller, J. Efficient iterative schemes for ab initio total-energy calculations using a plane-wave basis set. *Phys. Rev. B* **54**, 11169 (1996).

50. Kresse, G. & Furthmüller, J. Efficiency of ab-initio total energy calculations for metals and semiconductors using a plane-wave basis set. *Comput. Mater. Sci.* **6**, 15–50 (1996).

51. Perdew, J. P., Burke, K. & Ernzerhof, M. Generalized gradient approximation made simple. *Phys. Rev. Lett.* **77**, 3865 (1996).

52. Dion, M., Rydberg, H., Schroder, E., Langreth, D. C. & Lundqvist, B. I. Van der Waals density functional for general geometries. *Phys. Rev. Lett.* **92**, 246401 (2004).

53. Nosé, S. A unified formulation of the constant temperature molecular dynamics methods. *J. Chem. Phys.* **81**, 511–519 (1984).

54. Hoover, W. G. Canonical dynamics: equilibrium phase-space distributions. *Phys. Rev. A* **31**, 1695 (1985).

55. Martínez, L., Andrade, R., Birgin, E. G. & Martínez, J. M. PACKMOL: a package for building initial configurations for molecular dynamics simulations. *J. Comput. Chem.* **30**, 2157–2164 (2009).

Acknowledgements

Author contributions

Competing interests

Additional information